



# Turbulence Effect on Transpiration Cooling Effectiveness Over a Flat Plate in Hypersonic Flow and Sensitivity to Injection Parameters

Adriano Cerminara<sup>1</sup>

Received: 15 September 2022 / Accepted: 9 February 2023 / Published online: 3 March 2023  
© The Author(s) 2023

## Abstract

This work presents a numerical study of coolant porous injection in hypersonic turbulent boundary layer, with an analysis of blowing ratio and pore diameter effects on the cooling performance. Direct numerical simulations (DNS) are carried out for a Mach 5 flow over a flat plate with induced transition, and with a porous injection model to mimic injection from a bed of equally-spaced circular pores. The cooling performance in turbulent flow is compared to laminar 2D flow cases. Results show downstream development of a turbulent wedge-shaped structure, where a dramatic decay of the near-wall coolant concentration is observed. Blowing ratio and pore size are seen to affect the calmed and transitional regions, however they have a marginal or negligible effect within the turbulent region. A cooling effectiveness deficit/reduction of 15% to 30% for the turbulent cases, with respect to the laminar 2D cases, is observed above the injection region due to the 3D flow effects associated with the porous injection, whereas it reaches values as high as 80% in the developed turbulent region due to the turbulent convective effects. The present results shed light on the effects of turbulence on porous wall cooling and clearly indicate that alternative (ad-hoc) injection strategies and parameter calibration are needed to guarantee appropriate wall cooling in a turbulent flow.

**Keywords** Hypersonic flow · Turbulence · Film cooling · Transpiration cooling

## 1 Introduction

Hypersonic flight is characterised by extremely high values of the heat flux on the vehicle surface, and consequently surface temperatures that can reach values well above the tolerable limit of the structure. This is due to the aerodynamic heating phenomenon. For a cold isothermal wall, a hypersonic thermal boundary layer is characterised by a significantly high peak of the temperature profile near the wall, which is responsible for large values of the temperature gradient at the wall. This is due to the viscous effects within

---

✉ Adriano Cerminara  
a.cerminara@shu.ac.uk

<sup>1</sup> Department of Engineering and Mathematics, Sheffield Hallam University, Sheffield S1 1WB, UK

the boundary layer, and particularly to the dissipation of the large amounts of kinetic energy (from the hypersonic speeds at the boundary-layer edge to zero at the wall) into thermal energy, which generates a high local increase of the temperature within the boundary layer. If enough time is allowed for the wall temperature to increase due to the aeroheating towards the adiabatic conditions, and in an ideal case in which the wall temperature can increase continuously without any heat dissipation mechanisms, the wall would approach the so called recovery temperature, which is represented by the total temperature of the flow (a value significantly higher than the static temperature in the freestream due to the kinetic energy term contribution) decreased by the recovery factor. In addition to that, transition to turbulence contributes to dramatically increasing the heat flux, due to the enhanced mass and energy exchange within the boundary layer. To guarantee the vehicle structure integrity an effective cooling technique must be applied on the surface, which dissipates the intense heat loads and keeps the temperature within a tolerable value.

In the past decades, different cooling strategies have been investigated to address this problem. Film cooling (Fitt et al. 1985; Fitt and Wilmott 1994) is an active cooling technique in which a coolant flow is injected into the hot hypersonic boundary layer to suppress the wall heat flux by forming a coolant film adjacent to the surface. Two injection strategies can be considered, namely injection through localised holes, i.e. effusion cooling (Wittig et al. 1996; Baldauf et al. 2001), and through a porous structure, i.e. transpiration cooling (Meinert et al. 2001; Langener et al. 2011). The latter is considered more efficient due to the formation of a more homogeneous coolant film via the porous structure. Injection through two-dimensional slots, as opposed to localised holes, helps reducing the three-dimensional flow effects correlated with effusion cooling, hence delaying transition, which is of great importance in supersonic/hypersonic flows (Heufer and Olivier 2008; Keller et al. 2015; Keller and Kloker 2017). Transpiration cooling represents an innovative wall cooling technique with the potential to enable long-duration hypersonic cruise flight in virtue of its high efficiency. However, the mechanisms governing the cooling performance in a turbulent boundary layer, including the way key parameters of the porous structure and injection patterns affect the turbulent flow features, are still poorly understood. This makes difficult any tentative of an ad-hoc design of the porous structure for maximising the cooling effectiveness.

Meinert et al. (2001) reported data from experiments of foreign gas injection into turbulent boundary layers and empirical correlations showing a general good agreement with experimental results for skin-friction and heat-transfer profiles. They also considered numerical results for the solution of 2D turbulent boundary layers, using the mixing length hypothesis of van Driest to describe the turbulent viscosity, showing agreement with the empirical correlations. Gülhan and Braun (2011) considered experiments in both laminar and turbulent hypersonic flows, showing that the cooling efficiency is significantly higher in laminar flow than in turbulent flow. Hombsch and Olivier (2013) experimentally investigated film cooling in supersonic laminar and turbulent flows in the shock-tunnel facility TH2 at the Shock Wave Laboratory, RWTH Aachen University. They investigated the effect of different flow parameters, including Mach and Reynolds numbers, the blowing ratio, as well as various geometry parameters, like the blowing angle, slot width, and blowing holes. They considered two different injection configurations, namely injection through slots or through localised holes. Their data confirmed that film cooling in laminar flow is more efficient than in turbulent flow. These results are consistent with those from other studies, e.g. the numerical work of Keller and Kloker (2017), in which cooling through slot injection was simulated for different

gases in both laminar and turbulent conditions, and a significant reduction of the cooling effectiveness, particularly for air-into-air cooling, was found in turbulent conditions.

Brune et al. (2015) used RANS simulations to investigate the cooling effectiveness of transpiration cooling for both fully laminar and fully turbulent models of hypersonic flow over a two-dimensional blunt leading-edge geometry. Their results indicated a noticeable reduction of the cooling effectiveness for the turbulent case, compared to the laminar case. Christopher et al. (2020) studied the effects of transpiration cooling in a turbulent boundary layer for a low subsonic Mach number via DNS. They found a reduction in the cooling effectiveness due to the turbulent transport. The studies of Cerminara et al. (2020, 2021) have found that transpiration cooling performs better than slot injection when transition to turbulence occurs, as the transition process of slot injection has been observed to produce a larger dispersion of coolant away from the wall. However, the mechanisms through which the parameters of the porous structure and the injection patterns affect the mixing and the associated fluid dynamics features of the turbulent boundary layer have not been investigated yet. This, in turn, is crucial as it enables informed design and accurate calibration of the transpiration cooling system for optimal performance in both laminar and turbulent flows. The recent studies of Ifiti et al. (2022a, 2022b) presented a data set of 2D numerical and experimental results for transpiration cooling in a laminar hypersonic boundary layer.

Other strategies for the film cooling technique consist in wall-parallel and inclined blowing. In both cases a wall-parallel velocity component is provided to the injected coolant, which helps coolant staying closer to the wall, as observed in Linn and Kloker (2008). The recent work of Peter and Kloker (2022) investigated via DNS the effect of film cooling in a supersonic turbulent boundary layer with wall-parallel blowing through a backward facing step, for the thermal protection of the nozzle extension of rocket engines.

Although the above mentioned studies have provided many useful information on the characteristics of film cooling in turbulent flows, a lack of understanding is still present about the underlying physical mechanism of a coolant stream interacting with a transitional and turbulent boundary layer, as well as its correlated effects on the cooling effectiveness. This, in turn, is also associated with the still poor number of high-fidelity DNS data available for the case of transpiration cooling in a hypersonic turbulent flow. The main reasons for that consist in the computational time restrictions imposed by resolving the injection flow through a porous material, combined with the grid resolution level necessary to capture the compressible turbulent flow features outside of the porous material, and the relatively long domain sizes necessary to adequately predict the cooling-effectiveness trend from the injection location to the downstream flow regions. The present contribution addresses this problem making use of a model of porous injection imposed in DNS computations to mimic the blowing profile from a bed of equally-spaced circular pores. Moreover, rapid transition to turbulence is induced via application of an unsteady high-amplitude disturbance model upstream of the porous injection region, and the computational domain size is designed to accommodate a full transition process to a developed turbulent field at larger downstream distances from the injection region. The freestream conditions are the same as those considered in the works of Cerminara et al. (2020, 2021). The aim of the present study is to analyse the features of porous injection in a turbulent hypersonic boundary layer, with emphasis on the effects on the near-wall coolant concentration and the deficit in cooling effectiveness associated with a turbulent flow, as compared to a laminar flow case, as well as to analyse the solution sensitivity to important parameters of the porous injection model, namely blowing ratio and pore diameter.

## 2 Methodology

### 2.1 Governing Equations

The system of the three-dimensional dimensionless governing equations for compressible flow, written in conservation form, under the assumption of constant specific heats, is given in Cartesian coordinates as

$$\frac{\partial \rho}{\partial t} + \frac{\partial \rho u_j}{\partial x_j} = 0, \quad (1)$$

$$\frac{\partial \rho u_i}{\partial t} + \frac{\partial \rho u_i u_j}{\partial x_j} = -\frac{\partial p}{\partial x_i} + \frac{1}{\text{Re}} \frac{\partial \tau_{ij}}{\partial x_j}, \quad (2)$$

$$\frac{\partial \rho E}{\partial t} + \frac{\partial \left( \rho E + \frac{p}{\rho} \right) u_j}{\partial x_j} = \frac{1}{(\gamma - 1) \text{RePrM}^2} \frac{\partial}{\partial x_j} \left( \frac{\partial \mu T}{\partial x_j} \right) + \frac{1}{\text{Re}} \frac{\partial \tau_{ij} u_i}{\partial x_j}, \quad (3)$$

$$\frac{\partial \rho Y}{\partial t} + \frac{\partial}{\partial x_j} \left( \rho Y u_j - \frac{\mu}{\text{ReSc}} \frac{\partial Y}{\partial x_j} \right) = 0, \quad (4)$$

where Eq. (4) is the mass conservation equation for the coolant species, which is air in the considered case. The terms  $\rho$ ,  $\rho u$ ,  $\rho v$ ,  $\rho w$  and  $\rho E$ , and  $\rho Y$  are the conservative variables of the system of equations, where  $\rho$  is the density,  $u$ ,  $v$  and  $w$  are the velocity components respectively in the  $x$ -,  $y$ - and  $z$ -direction,  $E$  is the total energy per unit mass,  $Y$  is the coolant mass fraction, and the terms  $p$ ,  $T$ ,  $\tau_{ij}$  and  $\mu$  are respectively the pressure, temperature, viscous stress tensor components and dynamic viscosity. The physical variables are normalised through their freestream reference values, except for the pressure, which is normalised with the term  $\rho_\infty^* U_\infty^{*2}$ . The superscript (\*) is used to denote dimensional values. The characteristic length chosen to normalise the length scales is the boundary-layer displacement thickness ( $\delta^*$ ) of the similarity solution at the inflow. The characteristic fluid dynamic time is  $\delta^*/U_\infty^*$ . The terms Re, Pr, Sc, M and  $\gamma$  are respectively the Reynolds, Prandtl, Schmidt and Mach numbers, and the ratio of specific heats ( $\gamma = c_p^*/c_v^*$ ) for air, i.e. the dimensionless parameters of the flow. The Reynolds number is defined as  $\text{Re} = (\rho_\infty^* U_\infty^* \delta^*)/\mu_\infty^*$ ; the Prandtl number is set to 0.72, the Schmidt number is set to 1, and  $\gamma$  is equal to 1.4, for air. Sutherland's law is used to model the viscosity. Since the coolant gas species is the same as the species in the freestream, i.e. air, the ordinary mass diffusion term within the energy equation is zero. Thermal diffusion is neglected, as it was observed to be negligible if the species in a binary mixture have similar properties Keller et al. (2015).

### 2.2 Code Features

The code we use to carry out our DNS computations is the SBLI (shock-boundary-layer interaction) code, developed over a number of years at the University of Southampton. The code uses a fourth-order central finite-difference base scheme, for space discretisation, including the same-order boundary treatment (Carpenter et al. 1999), in combination with a second-order Harten-Yee total variation diminishing (TVD)-type shock-capturing scheme

(Yee et al. 1999), for the treatment of sharp gradient regions. Moreover, the code makes use of an entropy-splitting method (Sandham et al. 2002) to improve the nonlinear stability of the high-order central scheme. For time integration, a third-order Runge-Kutta scheme is used. The Harten-Yee shock-capturing scheme is equipped with the Harten's switch, a particular compression method (Yee et al. 1999) which concentrates the artificial dissipation to sharp gradient regions, thus providing minimum dissipation in the smooth regions. The code is also supplemented with the Ducros sensor (Ducros et al. 1999), which suppresses any residual artificial dissipation from the shock-capturing scheme in vortical regions (i.e. the boundary layer). A favourable feature of this sensor is that it does not require any a priori knowledge of the shock position. The code works using MPI libraries, and has been set up to run in parallel, by dividing the domain into a number of sub-domains, and assigning each of them to a particular processor. Validations of the code can be found in the work of De Tullio et al. (2013), where DNS results are compared with PSE results for the case of transition induced by a discrete roughness element in a boundary layer at Mach 2.5, and in Cerminara (2017) for different hypersonic flow configurations.

### 2.3 Computational Domain and Simulation Settings

A rectangular-box computational domain for a flat plate is considered, with dimensions  $L_x = 300$ ,  $L_y = 30$ , and  $L_z = 48$ . The mesh size in the different directions is  $N_x = 1874$ ,  $N_y = 201$ ,  $N_z = 360$ , and a grid stretching in the vertical direction towards the wall has been applied in order to accurately resolve the boundary layer. The present grid provides values of  $\Delta y^+ = 0.34$ ,  $\Delta x^+ = 8.2$ ,  $\Delta z^+ = 6.8$  at  $x = 250$  within the fully developed turbulent region, hence guaranteeing DNS resolution in all the directions, according to the work of Coleman and Sandberg (2010), being the thresholds 1, 15 and 8 for  $\Delta y^+$ ,  $\Delta x^+$  and  $\Delta z^+$ , respectively. The grid requirements also compare reasonably well with those described in the work of Yang et al. (2021) for capturing rare high-intensity wall shear stress events. In particular, a grid resolution requirement dependent on the friction-based Reynolds number is presented for both  $\Delta x^+$  and  $\Delta z^+$  in the work of Yang et al. (2021), and our considered values of  $\Delta x^+$  and  $\Delta z^+$  are within the threshold values indicated in Yang et al. (2021) for resolving 99 % of the wall shear-stress events at a calculated friction Reynolds number of  $Re_\tau = 325$ , based on the  $\delta_{99}$ , within the downstream turbulent region.

Simulations are carried out at the freestream Mach number  $M = 5$ , temperature  $T_\infty^* = 76.6$  K and Reynolds number  $Re = 12600$ , relative to the boundary-layer displacement thickness at the inlet, and for isothermal wall with wall temperature  $T_w^* = 290$  K. The freestream and wall temperature conditions are the same as in the studies (Cerminara et al. 2020, 2021), and are associated to the hypersonic wind-tunnel experiments of Hermann et al. (2018). Periodic conditions are imposed at the side boundaries. The flow is initialised with the similarity boundary-layer solution for a Mach 5 flow at the specified wall temperature, whereas extrapolation, integral and zero-gradient outflow conditions are set at the inlet, top and outlet boundaries, respectively. Porous injection is modelled through a spanwise and streamwise periodic function, consisting of an array of coolant jets with circular section, with imposed surface diameter and imposed blowing ratio. This model mimics a bed of equally-spaced injecting circular pores of the same size, which spans the whole domain width in the spanwise direction and extends from  $x = 55$  to  $x = 100$  in the streamwise direction. Coolant is injected at the same temperature of the wall, as in experimental conditions for short-duration wind-tunnel runs where both wall and coolant can be assumed at the room temperature Hermann et al. (2018). Air is considered as the coolant

fluid, which is the same species as the freestream fluid. It is assumed that the coolant exits the pores at the same pressure conditions as the local flow on the surface, thus mimicking a case in which the pressure drop across the underneath porous medium corresponds to the difference between the reservoir pressure and the external (or environmental) pressure on the surface Cerminara et al. (2020). Simulations have been run at three different values of the blowing ratio, i.e. the maximum value of the wall-normal momentum at the peak of each jet ( $F = \rho v_{inj,max}$ ), equally imposed on each pore, namely 0.003, 0.006 and 0.009, for a pore dimensionless diameter of 1.2. Furthermore, another simulation has been run at the blowing ratio of 0.003 and pore diameter 2.4, to evaluate the effect of doubling the pore size.

The wall-normal momentum component ( $\rho v_{inj}$ ) over the porous surface is modelled as follows,

$$\rho v_{inj}(x, z) = F \left| \sin^3 \left( x \frac{\pi}{D} \right) \sin^3 \left( z \frac{\pi}{D} \right) \right| \quad (5)$$

with  $D$  being the diameter of each pore. The present model represents a useful simplified way to mimic injection from a porous surface, which allows avoiding expensive simulation of the flow through the entire porous layer, considering that our intent is to simulate the effects in the outer flow of an assigned blowing ratio and of the characteristic pore geometrical parameters, namely shape and diameter. Moreover, it should be mentioned that the considered values of the blowing ratio correspond to relatively low values of the granular Reynolds number, based on the pore diameter and the averaged injection speed over the pore surface,  $Re_d = \rho \bar{v}_{inj} D / \mu$  (the highest value of the granular Reynolds number,  $Re_d = 16.4$ , is reached for the highest considered blowing ratio). As a result, a steady laminar flow of the jets at the surface is obtained, as was observed in previous studies at similar conditions (Cerminara et al. 2020). This, in turn, justifies a modelling approach for the porous injection profile, as opposed to the approach of simulating the inner porous medium flow.

The surface porosity associated with the present injection model is  $\epsilon = \pi/4$ , constant for both pore sizes. The main advantages of the above function for the blowing profile are represented by its simplicity and by the fact that the profile approaches the wall with an horizontal tangent, which prevents from generation of numerical oscillations that may arise in the neighbour grid points in cases of sharp variation in the first derivative. It should be mentioned, however, that different types of blowing distributions with sharp edges (e.g. a Poiseuille distribution) may be more appropriate for a higher accuracy of the injection profile, and that the particular distribution depends in general on the coolant flow conditions and the exact inner geometry of the pores. A more in-depth investigation on the effects of different blowing profile distributions on the cooling performance is addressed to future studies.

Figures 1 and 2 show the shape of the blowing profile imposed on the surface and a top view of the computational domain with contours of the coolant concentration, respectively. As can be seen, a wedge-shaped dark blue region extends from the end of the porous injection region to the outlet of the domain, which represents the turbulent wedge region, where a strong decrease of the coolant concentration at the surface is observed.

A previous numerical work (Cerminara et al. 2021) conducted at the same flow conditions and using similar main simulation settings, but for the case of injection through slots at different blowing ratios, showed a very good agreement with experimental data of Hermann et al. (2018), when moderate disturbances are imposed within the boundary layer.

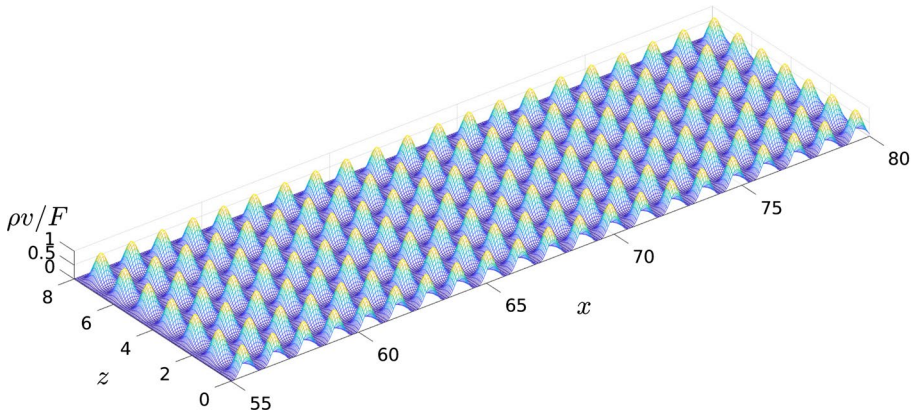


**Fig. 1** Blowing profile on the surface, contours of the normalised wall-normal momentum

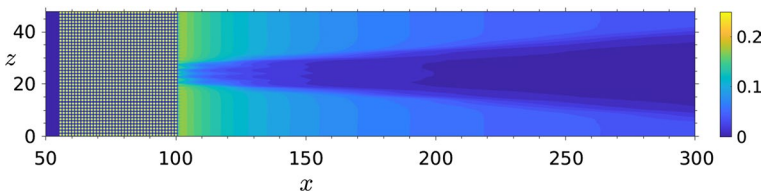


**Fig. 2** Top view of the time-averaged coolant concentration field on the surface, at  $F = 0.003$ , showing extent of computational domain in a  $xz$ -plane and the porous injection region

This, in turn, indicates the appropriateness of the simulation settings used for the present case.

High-amplitude disturbances are imposed upstream of the bed of pores to induce rapid transition to a developed turbulent flow downstream. The disturbance model described in (Cerminara et al. 2021) is applied to the spanwise velocity component (which induces three-dimensional effects leading to a rapid transition process). The disturbance waves are imposed on the surface between  $x = 10$  and  $x = 41$  in the streamwise direction, and between  $z = 20$  and  $z = 28$  in the spanwise direction, at an amplitude of  $w' = 2 \times 10^{-2}$ , and with imposed frequency, streamwise and (three multiple) spanwise wavenumbers corresponding to the most unstable modes (oblique first modes) computed through a previous LST study (Cerminara et al. 2021).

### 3 Results

#### 3.1 2D Laminar Flow

In this section we present results for the laminar 2D version of the considered configuration, with pore width of 1.2 in the streamwise direction. The domain length in this case is 200. By considering a row of pores at a generic  $z$  station in the 3D domain, the blowing profile in the 2D domain is taken as the wall-normal momentum profile along an

axis passing through the centre of each pore along the row of pores. Figures 3, 4 and 5 show contours of the coolant concentration in the injection region at the blowing ratios  $F = 0.003, 0.006, 0.009$ , respectively. As can be seen, at the lowest blowing ratio coolant is located within a narrow layer adjacent to the wall, whereas at the higher blowing ratios the local coolant concentration is significantly higher and the coolant layer increasingly thicker, thus proving the formation, as expected, of a consistent near-wall film of coolant (according to the principle of film cooling). Also, it can be observed that at increasing blowing ratios the coolant-rich region involves larger portions of the flow immediately upstream of the injection region (which starts at  $x = 55$ ). This is due to the higher blowing ratios producing a reverse flow region just upstream of the injection region, which convects coolant upstream, combined with a higher mass diffusion effect associated with larger local spatial concentration gradients.

Figure 6 shows the wall pressure distribution for at the different blowing ratios. A significant compression effect can be observed upstream of the injection region, as the boundary-layer thickness significantly increases as moving from the inlet to the injection region, due to the effect of the injected underneath layer of coolant. This results in a concave curvature of the boundary-layer edge upstream of the injection region, which, in turn, causes a compression of the outer supersonic flow. Then, once reached the start of the injection region, the curvature of the boundary layer edge reverses to a convex curvature, which results in an expansion of the supersonic flow along the streamwise direction above the injection region. This can be observed in Fig. 6, which shows that the pressure reaches a peak at about the start of the injection region, and then continuously decreases along the whole length of the injection region, assuming values slightly lower than the initial values at the inflow boundary just downstream of the injection region. As can be seen, the higher

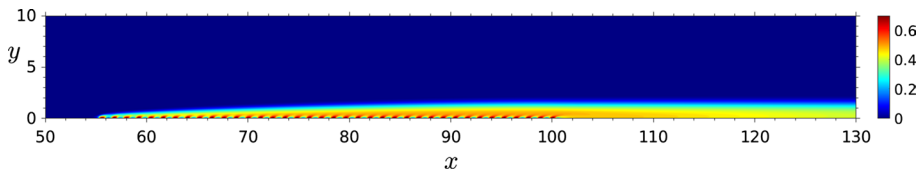


**Fig. 3** Coolant concentration field in the injection region,  $F = 0.003$

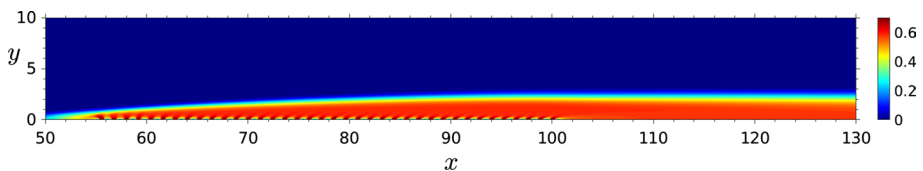


**Fig. 4** Coolant concentration field in the injection region,  $F = 0.006$

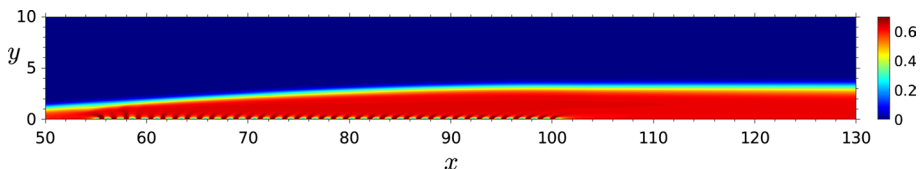


**Fig. 5** Coolant concentration field in the injection region,  $F = 0.009$



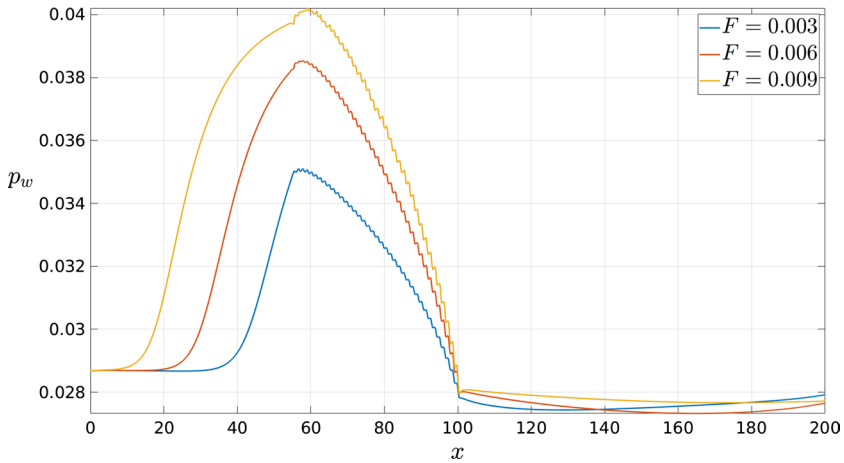


**Fig. 6** Wall pressure streamwise distribution

is the blowing ratio, the higher the streamwise extent of the high-pressure region as well as the pressure peak.

It should be mentioned that a decreasing streamwise profile of wall pressure above the injection region, as shown in Fig. 6, causes a corresponding increase of the injection velocity along the injecting surface. This is due to the fact that the density follows the same trend as the pressure, in virtue of the equation of state, with fixed wall temperature, which then results in an increase in the injection velocity for a constant imposed value of the blowing ratio.

Figure 7 shows contours of the temperature field at the highest blowing ratio ( $F = 0.009$ ), for which the previously-discussed compression and expansion effect is more pronounced than at the lower blowing ratios. Figure 7 highlights the increase of thickness of the boundary layer, from the inlet boundary and over the injection region, caused by coolant injection. As can be seen, upstream of the injection region the boundary-layer edge assumes a concave profile, which, as previously discussed, causes a compression in the supersonic flow, thus resulting in an increase of the temperature in the upper layers of the boundary layer. This can be observed also in Fig. 8, which shows the dimensionless surface heat-flux (in our simulation nondimensional system) profiles at the different blowing ratios in comparison with the case of no injection. The no-injection case represents the boundary-layer similarity solution. As can be seen, the three profiles corresponding to the different blowing ratios converge to the similarity

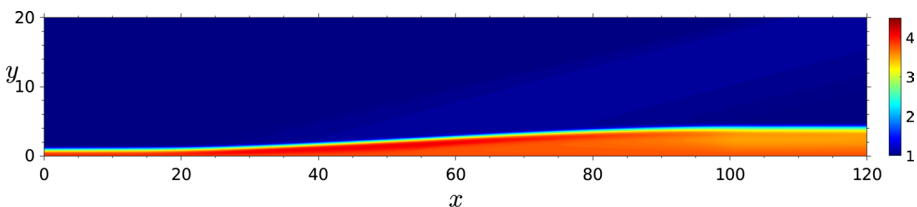


**Fig. 7** Temperature field in the injection region,  $F = 0.009$

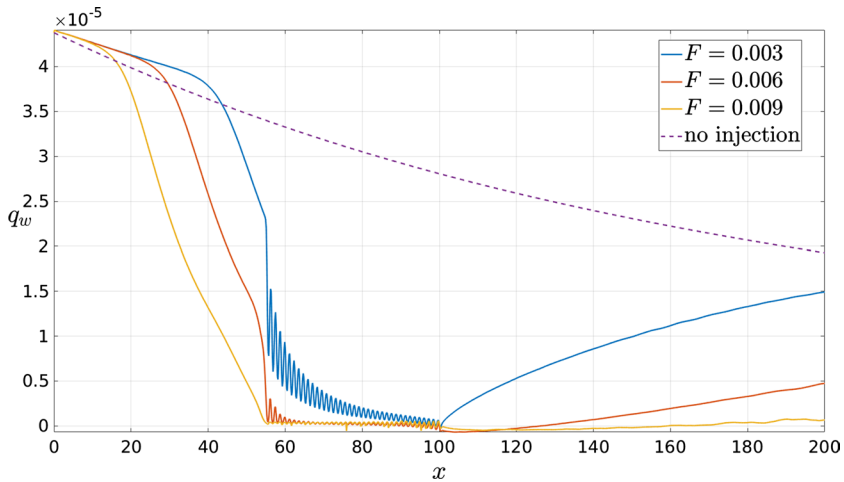


**Fig. 8** Wall heat-flux streamwise distribution

solution at the inlet. As moving towards the injection region, the heat-flux profiles show a slight increase first with respect to the laminar no-injection solution, which is due to the above-discussed supersonic compression behaviour, and then a rapid decrease indicating the entry point in the coolant zone of influence.

As previously discussed, at higher blowing ratios the coolant film involves larger portions of fluid upstream of the injection region, which can be seen in the earlier decrease of the heat-flux profiles in Fig. 8. Overall, it can be observed that the wall heat flux consistently decreases with increasing blowing ratios, both upstream and downstream of the injection region, as well as over the porous injection surface. This is as expected, since the mass of coolant injected from each pore per unit time is larger at larger blowing ratios, which increases the amount of coolant in the near-wall region. The oscillatory behaviour shown in the porous region is associated with the coolant jets from the surface. For all the profiles, the minimum value of the heat flux is approached near the exit of the injection region, then further downstream the heat-flux profiles start to increase again as they tend to recover the original laminar solution. At the lowest blowing ratio, the heat-flux increase downstream of the injection region is much more rapid and pronounced than the other blowing ratios, for which a more gradual increase is observed. At the highest blowing ratio, the heat flux keeps to values close to zero up to larger distances from the injection region, denoting very high cooling performance. Also, some oscillations can be observed in the profile for the highest blowing ratio, which are indicative of unsteadiness forming in the downstream flow due to the high blowing ratio.

Figure 9 shows the profiles of the cooling effectiveness along the surface at the different blowing ratios. As in Keller et al. (2015), the cooling effectiveness has been computed using the following formula

$$\eta = 1 - \frac{q_{w,c}}{q_{w,nc}}, \quad (6)$$

in which  $q_{w,c}$  represents the computed heat flux in the case with cooling, and  $q_{w,nc}$  is the heat flux without cooling.

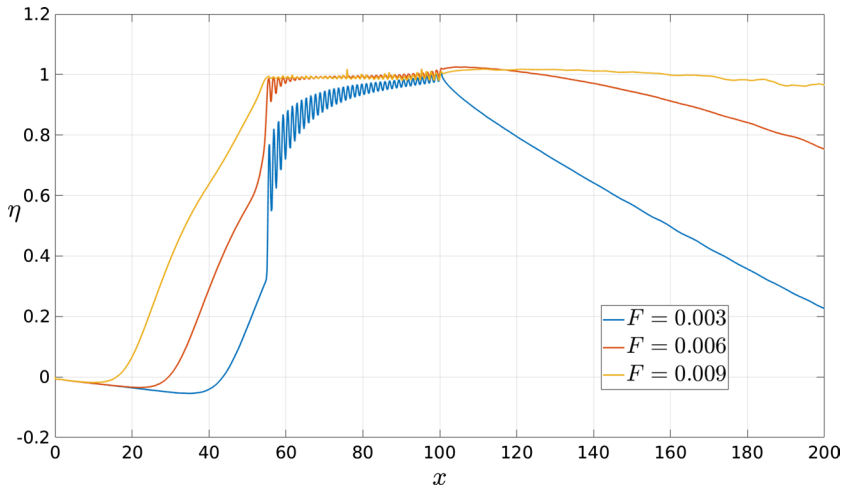


**Fig. 9** Cooling effectiveness streamwise distribution over the surface

Consistent with above discussion on the heat-flux profiles, it can be observed that higher values of cooling effectiveness are reached at larger blowing ratios; the cooling effectiveness profiles reach a maximum value of about 1 near the exit of the injection region for all the blowing ratios, then they gradually decay downstream. The decay for the lowest blowing ratio is much more rapid compared to the other blowing ratios. In contrast, for the highest blowing ratio, the decrease is very slow, with the cooling effectiveness keeping at a value close to 1 at larger distances from the injection region, up to the domain outlet.

Moreover, in Fig. 9 it can be noticed the presence of a localised region, just downstream of the injection zone, where the cooling effectiveness reaches values slightly above 1 for the higher blowing ratios ( $F = 0.006, 0.009$ ). This is due to a reversal of the wall heat flux, which, in turn, is associated with the effect of the coolant layer on the boundary-layer thickness over the injection region, and in particular to the convex curvature of the boundary-layer edge over the injection region. The convex curvature of the boundary-layer edge causes an expansion of the supersonic flow, as was previously described with reference to Fig. 6, with a resulting decrease of pressure and temperature. The latter reaches values slightly lower than the wall temperature in the immediate region downstream of the injection region, thus producing a local reversal of the temperature gradient at the wall.

## 3.2 3D Simulations with Transition to Turbulence

### 3.2.1 Effect of Blowing Ratio

Figures 10 and 11 show instantaneous temperature contours on a  $xz$ -plane at the height  $y = 1.4$  at the lowest and highest blowing ratios, respectively, whereas Fig. 12 shows the corresponding result at the height  $y = 0.44$  for the highest blowing ratio. As can be seen, the region above the bed of injecting pores is characterised by a rapid nonlinear growth of the boundary-layer disturbances and immediately downstream a breakdown process leading to the formation of the typical turbulent wedge structure, which develops further downstream. The temperature within the turbulent wedge assumes lower values compared to

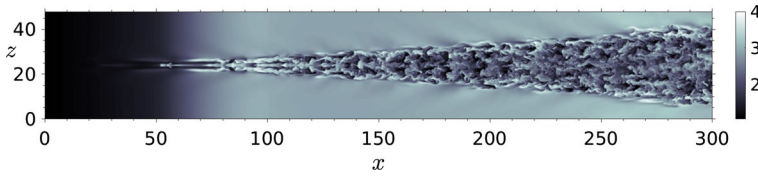


**Fig. 10** Instantaneous temperature field inside the boundary layer, at  $y = 1.4$ ,  $F = 0.003$

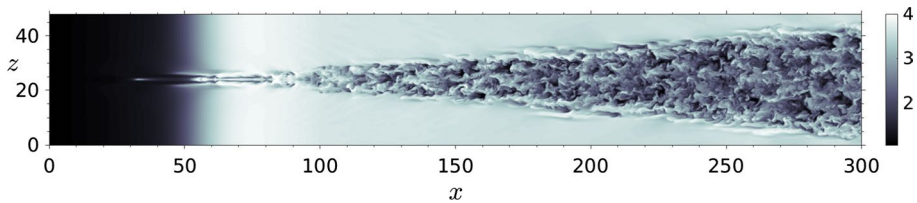


**Fig. 11** Instantaneous temperature field inside the boundary layer, at  $y = 1.4$ ,  $F = 0.009$

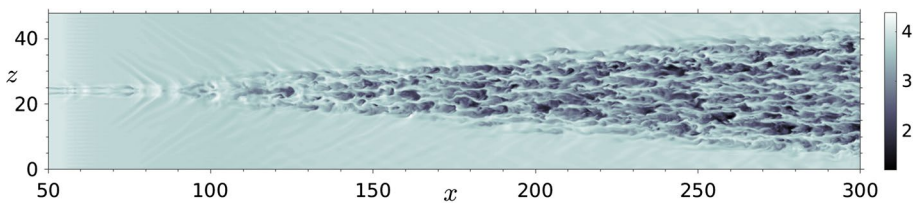


**Fig. 12** Instantaneous temperature field inside the boundary layer, at  $y = 0.44$ ,  $F = 0.009$

those outside of the wedge, i.e. within the calmed flow region, due to the flow recirculation which brings cold flow from the upper to the lower layers of the boundary layer. The wedge structure at the blowing ratio  $F = 0.009$  appears larger than for the case at  $F = 0.003$  in the spanwise direction, which indicates a more rapid growth of the turbulent wedge for higher blowing. The temperature contours in Fig. 12 at a lower distance from the wall show some different features compared to those observed in Fig. 11, both within and outside the turbulent wedge, including narrow streamwise-oriented streaky structures within the wedge, as well as the presence of oblique waves propagating from the sides of the turbulent wedge in the calmed flow region.

Figures 13, 14 and 15 show instantaneous cross-section temperature contours on  $yz$ -planes at the streamwise locations  $x = 100$ ,  $x = 200$  and  $x = 290$ , respectively, which indicate the different stages of the turbulent-wedge development process from the initial breakdown up to the fragmented boundary-layer structure reached further downstream. As can be observed, the boundary-layer fragmentation and randomisation spread along the spanwise direction as the wedge size grows laterally taking fluid from the calmed region inside the turbulent region.

Figures 16, 17, and 18 show the time-averaged temperature profiles within the boundary layer for the different blowing ratios, along the midspan axis ( $z = 24$ ) at the streamwise locations  $x = 100$ ,  $x = 200$ ,  $x = 290$ , respectively, downstream of the porous injection region. Figures 19, 20, 21 show the corresponding profiles of the streamwise

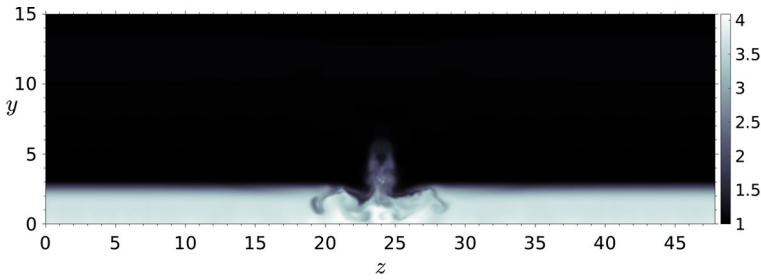


**Fig. 13** Instantaneous temperature field on a  $yz$ -plane at  $x = 100$ ,  $F = 0.009$

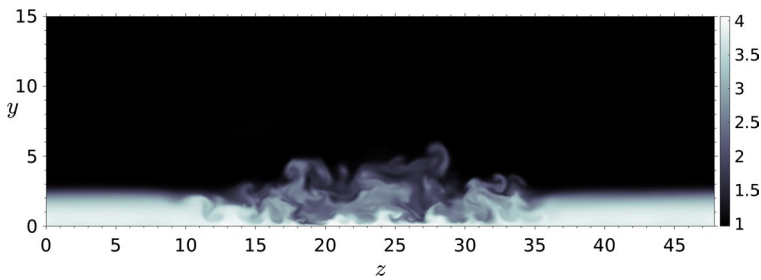


**Fig. 14** Instantaneous temperature field on a  $yz$ -plane at  $x = 200$ ,  $F = 0.009$

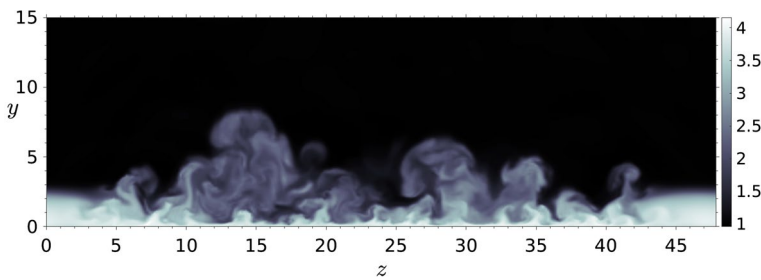


**Fig. 15** Instantaneous temperature field on a  $yz$ -plane at  $x = 290$ ,  $F = 0.009$

velocity component at the same streamwise locations. As can be seen, at the location  $x = 100$ , just downstream of the injection zone and in the early transition region, the differences in both the thermal and kinematic profiles at the different blowing ratios are more pronounced compared to the more downstream locations. The boundary layer appears significantly thicker at the higher blowing ratios, due to a thicker coolant layer injected by the porous surface, and a mixing layer region can distinctly be observed near the wall with evident inflection of both the temperature and velocity profiles, which is representative of the transition region between the air stream in the upper boundary layer and the underneath coolant layer adjacent to the wall. The thermal and kinematic profiles at the locations  $x = 200$  and  $x = 290$  show the development of the boundary layer in the turbulent region, in which larger temperature and velocity gradients are reached at the wall, and the differences between the different blowing ratios almost disappear due to the turbulent mixing. At both locations, the mixing layer is no longer

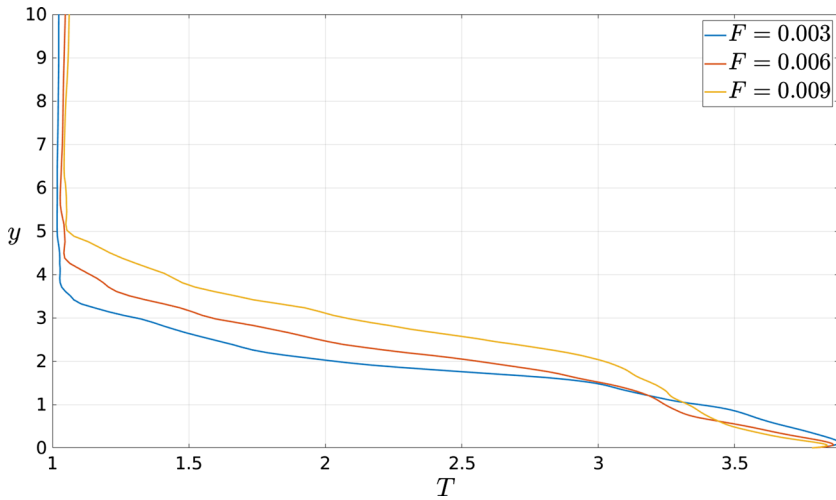


**Fig. 16** Time-averaged temperature profiles within the boundary layer at  $x = 100$  along the midspan axis

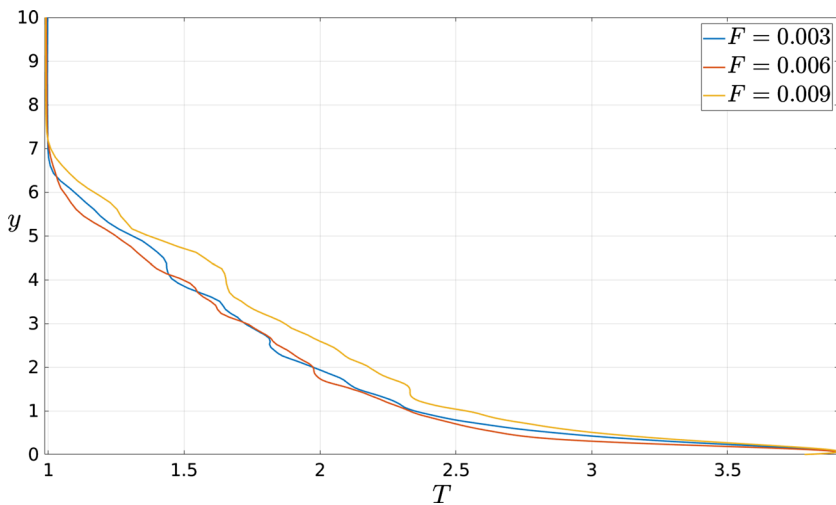
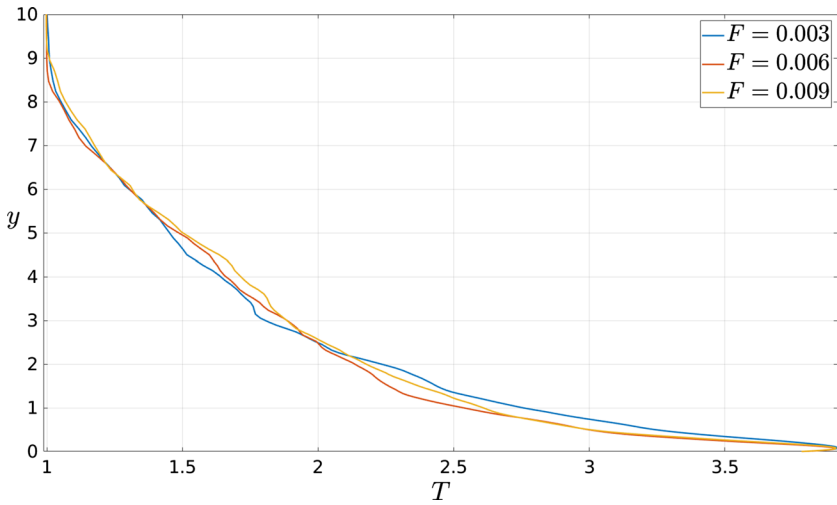


**Fig. 17** Time-averaged temperature profiles within the boundary layer at  $x = 200$  along the midspan axis

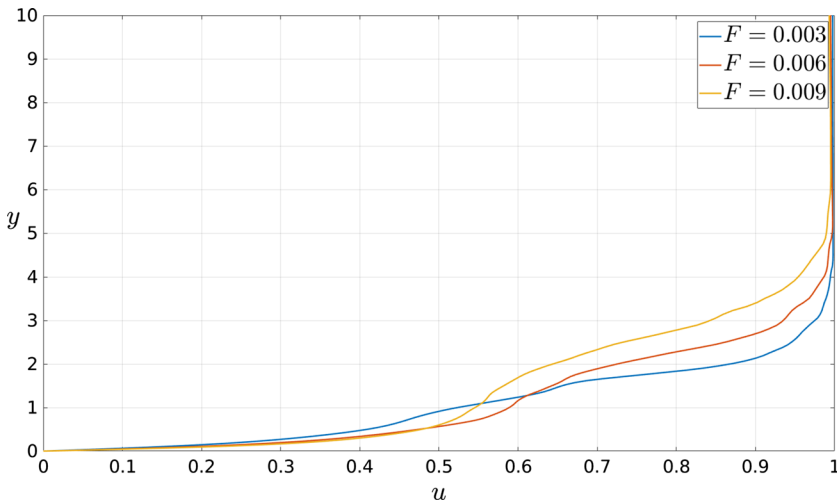
visible, as the coolant has been dispersed across the boundary-layer thickness through the turbulent convective effects and mixed with the fluid from the upper boundary-layer regions.

Figure 22 shows the time-averaged and spanwise-averaged surface heat-flux profiles within the turbulent wedge, at the different blowing ratios. The profiles are compared with the turbulent heat-flux prediction (no injection) obtained by application of the reference temperature method for the prediction of the Stanton number in turbulent compressible flows (Anderson 2006; Van Driest 1956).

The Stanton number is defined as



**Fig. 18** Time-averaged temperature profiles within the boundary layer at  $x = 290$  along the midspan axis



**Fig. 19** Time-averaged streamwise velocity profiles within the boundary layer at  $x = 100$  along the midspan axis

$$St = \frac{q_w^*}{\rho_\infty^* U_\infty^* c_p^* (T_{aw}^* - T_w^*)}, \tag{7}$$

and a prediction for compressible turbulent flow over a flat plate is given through Reynolds analogy as

$$St = \frac{c_f}{2s}, \tag{8}$$

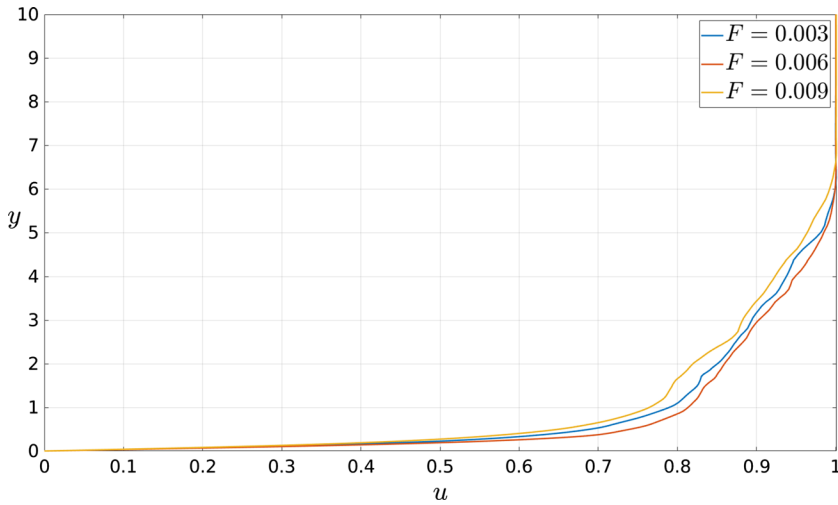


**Fig. 20** Time-averaged streamwise velocity profiles within the boundary layer at  $x = 200$  along the midspan axis

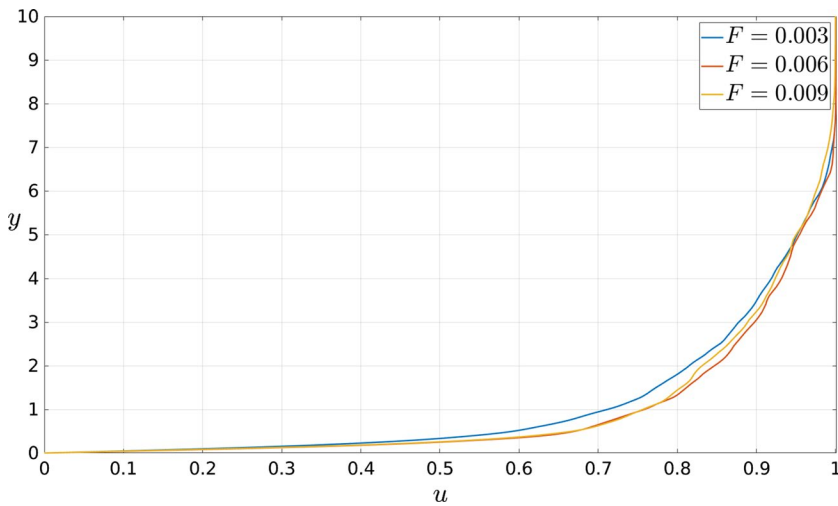


**Fig. 21** Time-averaged streamwise velocity profiles within the boundary layer at  $x = 290$  along the midspan axis

with the skin friction coefficient being expressed as

$$c_f = \frac{0.0592}{(Re_x)^{0.2}}, \tag{9}$$

where  $s$  coefficient is obtained from Van Driest’s correlations for turbulent flow (Van Driest 1956), and the Reynolds number  $Re_x$  is computed considering density and dynamic viscosity at a reference temperature, which is defined as (Anderson 2006)



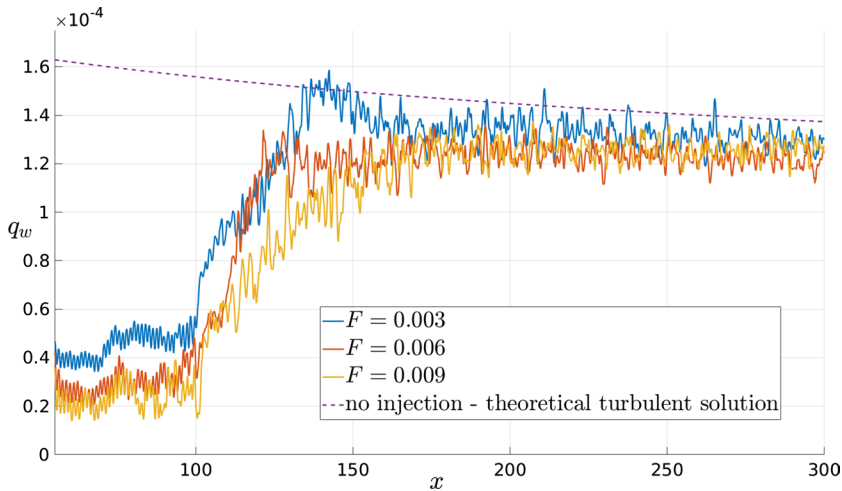


**Fig. 22** Time-averaged and spanwise-averaged wall heat-flux streamwise distribution

$$T_r = 1 + 0.032M^2 + 0.58(T_w - 1). \tag{10}$$

As can be observed in Fig. 22, increasing the blowing ratio from  $F = 0.003$  to  $F = 0.006$  provides a pronounced reduction of the heat-flux peak at the upper limit of the transition region (extending approximately from  $x = 100$  to  $x = 150$ ); an increase to  $F = 0.009$  provides a further decrease of the heat flux within the transition region and a more gradual variation from the laminar value to the turbulent value. However, the heat-flux profiles for the different blowing ratios collapse to a similar value in the developed turbulent flow region downstream. Furthermore, the profiles within the turbulent wedge are seen to approach the predicted turbulent heat-flux value with no injection, thus suggesting that the cooling effects have drastically reduced to values almost negligible in the turbulent region. This is consistent with the very low values shown by the time- and spanwise- averaged coolant concentration profiles over the surface within the turbulent wedge, depicted in Fig. 23. In particular, it can be observed that the concentration profiles undergo a rapid decay in the transitional region (contextually to the rapid increase of the heat flux), and then converge to a similar value downstream in the developed turbulent region, which is about an order of magnitude lower compared to the value just downstream of the porous injection region.

Figure 24 shows profiles of the cooling effectiveness for the turbulent case at the different blowing ratios, compared with the corresponding profiles for the laminar 2D case (plotted in Fig. 9). The cooling effectiveness for the turbulent profiles has been computed through Eq. (6), using the turbulent heat-flux prediction profile (no injection) for  $q_{w,nc}$ , and the corresponding time- and spanwise- averaged wall heat-flux profiles within the turbulent region at the different blowing ratios for  $q_{w,c}$ . As can be seen, above the injection region the cooling effectiveness for the 3D cases is lower by about 20 % to 30 % (dependent on the blowing ratio) with respect to the corresponding 2D laminar cases, however, the profiles in the transition region rapidly decay up to reaching values dramatically lower than the laminar cases further downstream in the developed turbulent region. The reduction of cooling effectiveness with respect to the 2D case over the

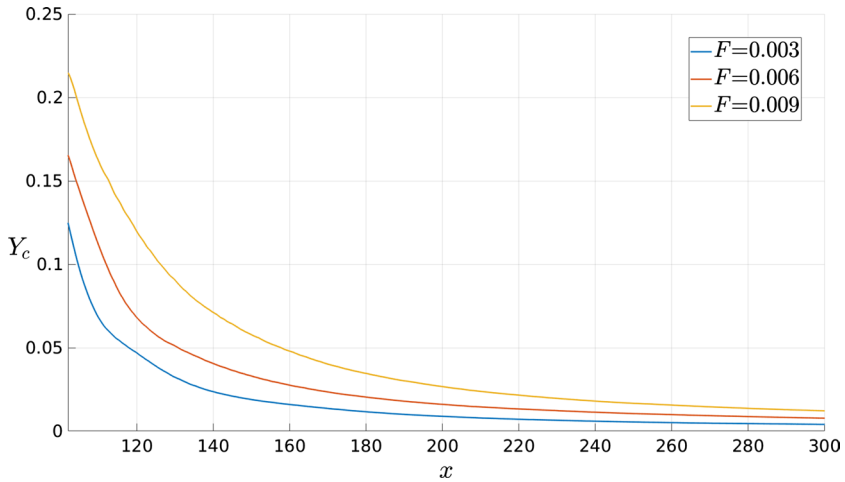


**Fig. 23** Time-averaged and spanwise-averaged coolant concentration streamwise distribution over the surface

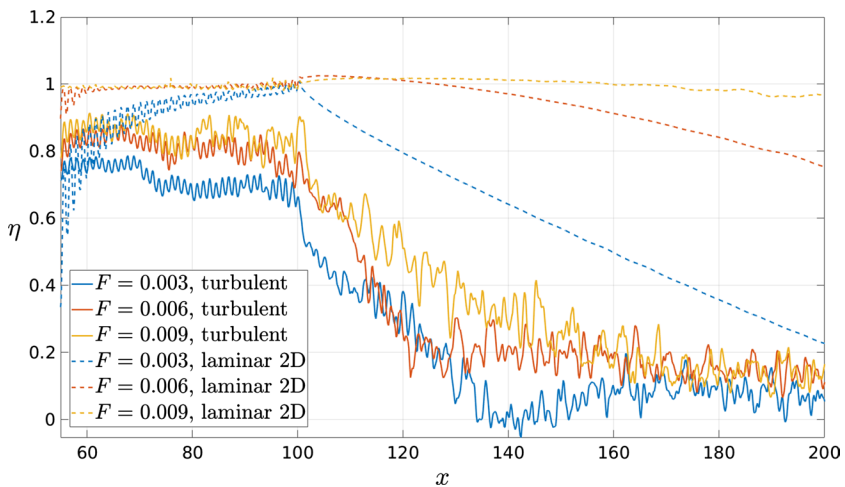


**Fig. 24** Cooling effectiveness streamwise distribution over the surface

porous surface is due to the two-dimensionality of the flow in the 2D case, rather than to transitional or turbulent flow features of the 3D cases. In fact, transition to turbulence occurs only downstream of the injection region, however the 3D porous pattern (and particularly the  $z$ -wise spacing between adjacent pores) provides a reduction in cooling effectiveness compared to a 2D case, in which the injecting jets corresponds to slots with infinite length (and hence continuous injection) in the spanwise direction. By computing the relative error between the laminar 2D and turbulent values of the cooling effectiveness, i.e.  $d = (\eta_l - \eta_t)/\eta_l$ , we obtain an estimation of the reduction (or deficit) of cooling effectiveness associated with the turbulent flow, with respect to a 2D laminar injection case. The results for the cooling-effectiveness deficit are plotted in Fig. 25,

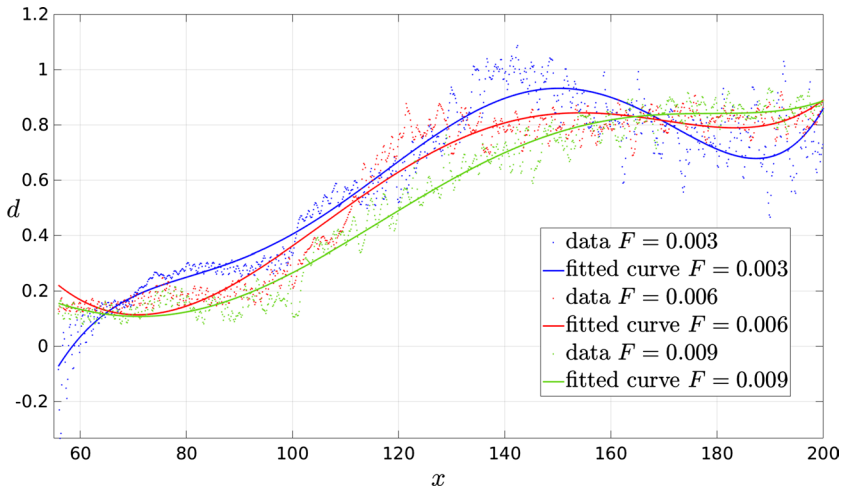


**Fig. 25** Streamwise distribution of the deficit of cooling effectiveness of the turbulent cases, with respect to the laminar 2D cases

where the simulation data, taken at each point in the streamwise direction from the start of the injection region ( $x = 55$ ) to the outlet of the laminar 2D cases ( $x = 200$ ), are fitted through a fifth-order polynomial (using the polynomial curve fitting technique in MATLAB). It can be observed the maximum deficit value is reached at the lowest blowing ratio and at approximately the position  $x = 140$ , where a reduction of about 100% of the corresponding laminar 2D value is observed. The profile at the lowest blowing ratio shows then a visible deficit reduction, due to a slight increase of the turbulent cooling effectiveness and contextually the consistent decrease of the cooling effectiveness in the laminar 2D case (as shown in Fig. 24), before increasing again further downstream. The profiles at the higher blowing ratios follow a similar trend, however the growth appear more gradual at increasing blowing ratio and a lower peak is reached, whereas a higher value is approached downstream of  $x = 170$ . Overall, we can conclude that a deficit in cooling effectiveness approximately between 15 % to 30 % (from highest to lowest  $F$ ) is observed over the porous region, compared to the corresponding laminar 2D cases, which is due to the above-mentioned two-dimensional pore effect in the 2D case. Then, downstream of the injection region, the turbulent cases show a consistent increase of the deficit in the transitional region up to the developed turbulent region where average deficit values of about 70 % to 85 % (from lowest to highest  $F$ ) are reached.

### 3.2.2 Effect of Pore Diameter

Two cases with different nondimensional pore diameters are considered, namely  $D = 1.2$  and  $D = 2.4$ , at the blowing ratio  $F = 0.003$ . Figures 26 and 27 show time-averaged contours of the coolant concentration on the surface for both pore diameters. As can be observed, the coolant concentration just downstream of the pores is higher for the larger pore size, and forms pronounced streaky structures, whereas it appears more uniform for the lower pore size. Figure 28 shows instantaneous contours of coolant concentration at the distance  $y = 0.44$  from the wall (at  $D = 1.2$ ), which highlights details of the coolant mixing features within the boundary layer. The coolant coming from the coolant-rich (i.e. the

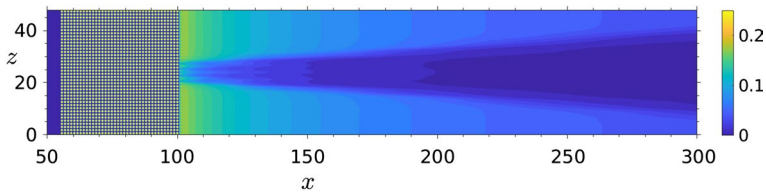


**Fig. 26** Time-averaged contours of coolant concentration over the surface,  $D = 1.2$

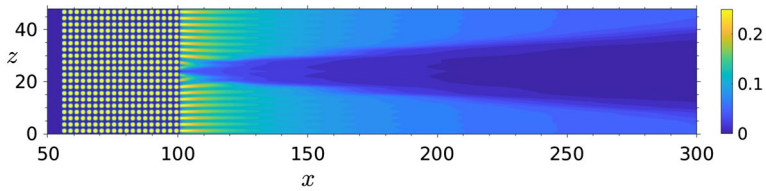


**Fig. 27** Time-averaged contours of coolant concentration over the surface,  $D = 2.4$

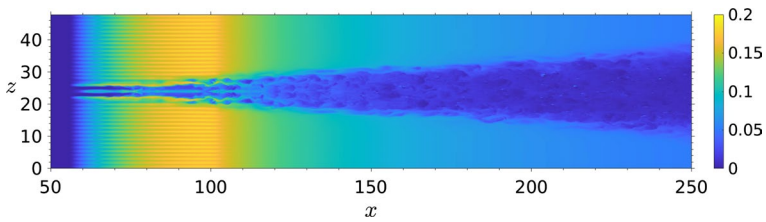
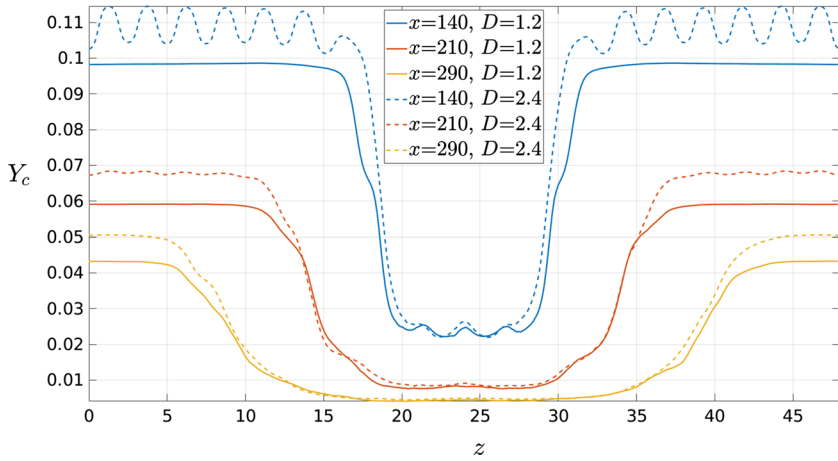


**Fig. 28** Instantaneous coolant concentration at  $y=0.44$  within the boundary layer ( $D = 1.2$ )

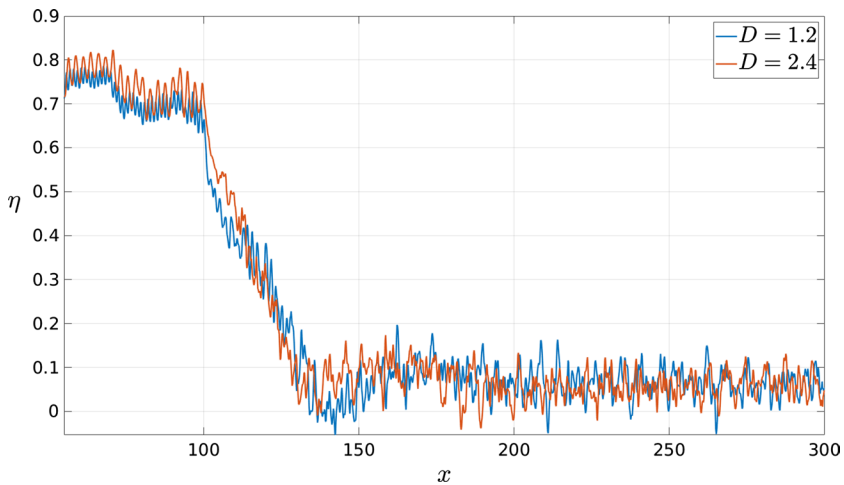
laminar) region appears to mix with the turbulent flow more effectively in the region just downstream of the pores ( $x > 100$ ), however it gradually decays in the downstream region as the turbulent wedge spreads in the spanwise direction.

Figure 29 shows profiles of the coolant concentration over the surface in the spanwise direction, at different  $x$  stations, for the different pore size cases. As can be seen, the coolant concentration decays rapidly as moving from the calmed (at the sides) to the turbulent region, and values in the calmed flow region are higher for the higher pore size, whereas converge to approximately the same value in the turbulent region for both pore sizes. The dramatic decay of the coolant concentration within the turbulent wedge is due to the turbulent convection effects that tend to take coolant off the wall, redistributing it within the boundary layer and mixing it with fluid coming from the upper regions, in other words disrupting the film of near-wall coolant. In contrast, in the adjacent calmed flow region the film of coolant over the surface is maintained up to higher downstream distances. Moreover, pronounced oscillations, with same wavelength as the pore diameter, are formed within the calmed flow region for the higher pore-size case, as opposed to a flatter profile shown by the smaller pore-size case. These oscillations are representative of the streaky structures observed in Fig. 27.

Figure 30 shows profiles of the cooling effectiveness for the different pore diameter cases. It can be observed that the cooling effectiveness is slightly higher for the larger pore



**Fig. 29** Time-averaged coolant concentration spanwise distribution at different  $x$  stations downstream of the injection region



**Fig. 30** Cooling effectiveness streamwise distribution over the surface

size within the injection region, whereas it shows an almost negligible effect in the transitional and turbulent regions, where the profiles converge to very similar values for both pore diameters.

### 4 Conclusion

The results presented in this work have shown the effect of the coolant blowing ratio and pore diameter on the wall heat flux and cooling effectiveness in a hypersonic turbulent boundary layer, and, contextually, the effect of turbulent transition on the coolant film adjacent to the wall for transpiration cooling applications. Due to imposed high-amplitude

disturbances on the surface, a turbulent wedge rapidly develops downstream of the porous injection region. Increasing the blowing ratio has been shown to produce a relevant reduction of the heat flux peak and gradient within the transitional region. However, at the same time, the blowing ratio has been observed to be almost ineffective at larger downstream distances from the injection location within the turbulent wedge, where the coolant concentration over the surface dramatically decays as a result of the turbulent convective effects. In contrast, in the adjacent calmed flow region, the film of coolant in direct contact with the surface is seen to develop up to larger downstream distances.

A comparison of the turbulent cases with laminar 2D simulations has proved that the cooling effectiveness for the laminar cases is significantly higher than for the turbulent cases, for each blowing ratio, in both the injection, transitional and turbulent flow regions. In particular, the turbulent cases show a deficit of the cooling effectiveness approximately between 15 % to 30 % (from highest to lowest blowing ratio) over the porous region, compared to the corresponding laminar 2D cases, which is associated with the 3D flow effects in the porous injection region. Then a consistent increase of the cooling-effectiveness deficit is observed in the transitional region up to the developed turbulent region where an average deficit of about 70 % to 85 % (from lowest to highest blowing ratios) is shown, which represents the result of the coolant dispersion within the boundary layer due to the turbulent convective effects.

Moreover, it was found that the effect of doubling the pore diameter produces relevant differences in the flow patterns near the porous region and within the calmed flow region, with higher observed levels of the coolant concentration. However, doubling the pore diameter provides almost negligible differences inside the turbulent wedge, where the cooling performance are strongly reduced due to the turbulent convective transport that increasingly reduces the values of coolant concentration at the wall as the wedge spreads laterally.

**Acknowledgements** Computer time on the UK National Supercomputing Service ARCHER 2 has been provided by the UK Turbulence Consortium (UKTC), under EPSRC (Engineering and Physical Sciences Research Council) grant no. EP/D44073/1, and EP/G06958/1. The present work has been carried out in the scope of the NATO AVT-352 Task Force “Measurement, Modelling and Prediction of Hypersonic Turbulence”.

**Author Contributions** A.C. conceptualised the work, obtained and analysed the data, wrote the main manuscript text, prepared the figures, and reviewed the manuscript

**Funding** The present work received support through computer time on the UK National Supercomputing Service ARCHER 2, provided by the UK Turbulence Consortium (UKTC) under EPSRC (Engineering and Physical Sciences Research Council) grant no. EP/D44073/1, and EP/G06958/1. No further funding is associated with the present work.

## Declarations

**Conflict of interest** The author declares they have no conflict of interest.

**Ethical approval** Not applicable.

**Informed consent** Not applicable.

**Open Access** This article is licensed under a Creative Commons Attribution 4.0 International License, which permits use, sharing, adaptation, distribution and reproduction in any medium or format, as long as you give appropriate credit to the original author(s) and the source, provide a link to the Creative Commons licence, and indicate if changes were made. The images or other third party material in this article are included in the article’s Creative Commons licence, unless indicated otherwise in a credit line to the material. If material is not included in the article’s Creative Commons licence and your intended use is not

permitted by statutory regulation or exceeds the permitted use, you will need to obtain permission directly from the copyright holder. To view a copy of this licence, visit <http://creativecommons.org/licenses/by/4.0/>.

## References

- Anderson, J.D.: Hypersonic and High-Temperature Gas Dynamics, 2nd edn, AIAA Education Series (2006)
- Baldauf, S., Schulz, A., Wittig, S.: High-resolution measurements of local heat transfer coefficients from discrete hole film cooling. *J. Turbomach.* **123**(4), 749–757 (2001)
- Brune, A., Hosder, S., Gulli, S., Maddalena, L.: Variable transpiration cooling effectiveness in laminar and turbulent flows for hypersonic vehicles. *AIAA J.* **53**(1), 176–189 (2015)
- Carpenter, M.H., Nordström, J., Gottlieb, D.: A stable and conservative interface treatment of arbitrary spatial accuracy. *J. Comput. Phys.* **148**(2), 341–365 (1999)
- Cerminara, A.: Boundary-layer receptivity and breakdown mechanisms for hypersonic flow over blunt leading-edge configurations (Doctoral dissertation, University of Southampton) (2017)
- Cerminara, A., Deiterding, R., Sandham, N.: A mesoscopic modelling approach for direct numerical simulations of transition to turbulence in hypersonic flow with transpiration cooling. *Int. J. Heat Fluid Flow* **86**, 108732 (2020)
- Cerminara, A., Hermann, T., Ifti, H.S., Deiterding, R., Sandham, N., McGilvray, M.: Influence of instability modes on cooling performance in hypersonic boundary layer with slot injection. *Aerosp. Sci. Technol.* **109**, 106409 (2021)
- Christopher, N., Peter, J.M., Kloker, M.J., Hickey, J.P.: DNS of turbulent flat-plate flow with transpiration cooling. *Int. J. Heat Mass Transf.* **157**, 119972 (2020)
- Coleman, G.N., Sandberg, R.D.: A primer on direct numerical simulation of turbulence—methods, procedures and guidelines (2010)
- De Tullio, N., Paredes, P., Sandham, N.D., Theofilis, V.: Laminar-turbulent transition induced by a discrete roughness element in a supersonic boundary layer. *J. Fluid Mech.* **735**, 613–646 (2013)
- Ducros, F., Ferrand, V., Nicoud, F., Weber, C., Darracq, D., Gacherieu, C., Poinsot, T.: Large-eddy simulation of the shock/turbulence interaction. *J. Comput. Phys.* **152**(2), 517–549 (1999)
- Fitt, A.D., Wilmott, P.: Slot film cooling—the effect of separation angle. *Acta Mech.* **103**(1), 79–88 (1994)
- Fitt, A.D., Ockendon, J.R., Jones, T.V.: Aerodynamics of slot-film cooling: theory and experiment. *J. Fluid Mech.* **160**, 15–27 (1985)
- Gülhan, A., Braun, S.: An experimental study on the efficiency of transpiration cooling in laminar and turbulent hypersonic flows. *Exp. Fluids* **50**(3), 509–525 (2011)
- Hermann, T., Ifti, H.S., McGilvray, M., Doherty, L., Geraets, R.P.: Mixing characteristics in a hypersonic flow around a transpiration cooled flat plate model (2018)
- Heufer, K.A., Olivier, H.: Experimental and numerical study of cooling gas injection in laminar supersonic flow. *AIAA J.* **46**(11), 2741–2751 (2008)
- Hombsch, M., Olivier, H.: Film cooling in laminar and turbulent supersonic flows. *J. Spacecr. Rockets* **50**(4), 742–753 (2013)
- Ifti, H.S., Hermann, T., McGilvray, M., Merrifield, J.: Numerical simulation of transpiration cooling in a laminar hypersonic boundary layer. *J. Spacecr. Rockets* **59**(5), 1726–1735 (2022)
- Ifti, H.S., Hermann, T., Ewenz Rocher, M., Doherty, L., Hambidge, C., McGilvray, M., Vandeperre, L.: Laminar transpiration cooling experiments in hypersonic flow. *Exp. Fluids* **63**(6), 1–14 (2022)
- Keller, M.A., Kloker, M.J.: Direct numerical simulation of foreign-gas film cooling in supersonic boundary-layer flow. *AIAA J.* **55**(1), 99–111 (2017)
- Keller, M.A., Kloker, M.J., Olivier, H.: Influence of cooling-gas properties on film-cooling effectiveness in supersonic flow. *J. Spacecr. Rockets* **52**(5), 1443–1455 (2015)
- Langener, T., Von Wolfersdorf, J., Steelant, J.: Experimental investigations on transpiration cooling for scramjet applications using different coolants. *AIAA J.* **49**(7), 1409–1419 (2011)
- Linn, J., Kloker, M.J.: Numerical investigations of film cooling. In: *RESPACE-Key Technologies for Reusable Space Systems* (pp. 151–169). Springer, Berlin, Heidelberg (2008)
- Meinert, J., Huhn, J., Serbest, E., Haidn, O.J.: Turbulent boundary layers with foreign gas transpiration. *J. Spacecr. Rockets* **38**(2), 191–198 (2001)
- Peter, J.M.F., Kloker, M.J.: Direct numerical simulation of supersonic turbulent flow with film cooling by wall-parallel blowing. *Phys. Fluids* **34**(2), 025125 (2022)
- Sandham, N.D., Li, Q., Yee, H.C.: Entropy splitting for high-order numerical simulation of compressible turbulence. *J. Comput. Phys.* **178**(2), 307–322 (2002)
- Van Driest, E. R.: The problem of aerodynamic heating. Institute of the Aeronautical Sciences (1956)

- Wittig, S., Schulz, A., Gritsch, M. Thole, K.A.: Transonic film-cooling investigations: effects of hole shapes and orientations. In: Turbo Expo: Power for Land, Sea, and Air, vol. 78750, p. V004T09A026. American Society of Mechanical Engineers (1996)
- Yang, X.I., Hong, J., Lee, M., Huang, X.L.: Grid resolution requirement for resolving rare and high intensity wall-shear stress events in direct numerical simulations. *Phys. Rev. Fluids* **6**(5), 054603 (2021)
- Yee, H.C., Sandham, N.D., Djomehri, M.J.: Low-dissipative high-order shock-capturing methods using characteristic-based filters. *J. Comput. Phys.* **150**(1), 199–238 (1999)